

COLORS OF DWARF ELLIPTICALS FROM *GALEX* TO *WISE*

JAMES M. SCHOMBERT^{A,B}

^ADepartment of Physics, University of Oregon, Eugene, OR USA 97403 and
^Bjschombe@uoregon.edu

Draft version March 11, 2022

ABSTRACT

Multi-color photometry is presented for a sample of 60 dwarf ellipticals (dE) selected by morphology. The sample uses data from *GALEX*, SDSS and *WISE* to investigate the colors in filters *NUV*, *ugri* and *W1* ($3.4\mu\text{m}$). We confirm the blueward shift in the color-magnitude relation for dwarf ellipticals, compared to CMR for bright ellipticals, as seen in previous studies. However, we find the deviation in color across the UV to near-IR for dE's is a strong signal of a younger age for dwarf ellipticals, one that indicates decreasing mean age with lower stellar mass. Lower mass dE's are found to have mean ages of 4 Gyrs and mean $[\text{Fe}/\text{H}]$ values of -1.2 . Age and metallicity increase to the most massive dE's with mean ages similar to normal ellipticals (12 Gyrs) and their lowest metallicities ($[\text{Fe}/\text{H}] = -0.3$). Deduced initial star formation rates for dE's, combined with their current metallicities and central stellar densities, suggests a connection between field LSB dwarfs and cluster dE's, where the cluster environment halts star formation for dE's triggering a separate evolutionary path.

1. INTRODUCTION

Ellipticals represent one of the most carefully studied type of galaxies with respect to stellar populations. They exhibit the simplest morphological as well as internal kinematics and, thus, are well-modeled as a single stellar population rather than the kinematically distinct components found in disk galaxies. They have the highest masses (i.e., luminosities) of all galaxy types and, therefore, are the clearest signposts at high-redshift. Studies of galaxy evolution often focus on ellipticals owing to early indications that their spectrophotometric changes are the simplest to model and trace, reliability, through cosmic time (so-called passive evolution). In addition, ellipticals are the only morphological type that inhabits every galaxy environment from the richest clusters to the field, and present a coherent appearance from the dwarf ellipticals to the brightest cluster members.

The study of stellar populations in ellipticals has historically taken three different routes. The first is the use of optical and near-IR colors to interpret the integrated light of the underlying stellar population. The discovery of the color-magnitude relation (CMR, Sandage & Visvanathan 1978), the separation of morphology types by color (Tojeiro *et al.* 2013) and different galaxy components by color (e.g., core versus envelope, Head *et al.* 2014) were often our earliest explorations into the stellar populations and the meaning of color with respect to the star formation history of galaxies (Tinsley 1978). Technological improvements in the 1980's led to a second, and obvious, extension of multi-color work through a higher resolution of the spectroenergy distribution (SED) of galaxies with the focus on various spectral indices related to different types of stars found in a stellar population. This type of investigation reached a peak with the development of the Lick/IDS line-strength system (Worthey *et al.* 1994; Trager *et al.* 2000) where a set of specific spectral features were shown to correlate with the two primary characteristics of a stellar population, its age and mean metallicity. Guided by SED models of

the Lick/IDS line-strength system (see Graves & Schiavon 2008), these spectral indices became the observable of choice to study nearby and distant galaxy stellar populations. Lastly, with the launch of HST, space imaging provide the best study of a stellar population by direct examination of their color-magnitude diagrams. The number of pure ellipticals open to HST CMD imaging is limited to the nearby Universe and, therefore, for a majority of stellar population studies the Lick/IDS line-strength system is the method of choice.

The use of optical and near-IR colors for investigating stellar populations still has a useful role to play even in the spectroscopic era. For example, higher signal-to-noise is acquired for faint, distant galaxies using colors. Large areal surveys, such as those obtained by wide-field cameras using well chosen filter sets, provide numerically superior datasets to spectroscopic surveys. In the 1990's, Rakos & Schombert pioneered the use of narrow band filters selected to cover age/metallicity features around the 4000\AA break as an fast and efficient system to study cluster galaxies with direct imaging (see Rakos & Schombert 1995). The results from those studies confirmed a passive evolution for the stellar populations in cluster ellipticals, but was in sharp disagreement with the results from spectroscopic surveys that found much younger ages and lower metallicities for the same objects (Trager *et al.* 2000; Graves *et al.* 2009; Conroy *et al.* 2014). Larger SDSS samples (Bernardi *et al.* 2005, Gallazzi *et al.* 2005; Graves, Faber & Schiavon 2010) presented a more diverse range of ages and metallicities, and more sophisticated analysis techniques (see Johansson *et al.* 2012; Conroy *et al.* 2014; Worthey *et al.* 2014), all of which reinforced the conclusion of younger ages and lower metallicities with decreasing luminosity and stellar mass for bright ellipticals.

One deficiency in spectroscopic surveys is that they are less able to explore low luminosity/mass realm of ellipticals, the dwarf ellipticals. Their combined low absolute luminosities and depressed central surface brightnesses made spectroscopic observations of dwarf ellipti-

calls a particular challenge even for nearby clusters and, in practice, impossible for high-redshift systems. Given the various scenarios where bright ellipticals are constructed from low mass systems by hierarchical mergers (Driver 2010), a deficiency in accurate stellar populations values (e.g., age and metallicity) for dwarf ellipticals is a continuing problem in comparing observations with theory.

This paper attempts to extend our knowledge of stellar populations in low mass systems by presenting a comprehensive analysis of dwarf elliptical colors using archival data from the near-UV (*GALEX NUV*) to the far-IR (*WISE* $3.4\mu\text{m}$) in an effort to extend our estimates of age and metallicity to the low mass realm. This study is an extension of the color analysis of bright ellipticals ($M_g < -20$) from Schombert (2016) that focuses on presenting a large sample of morphologically classified dwarf ellipticals (class dE) and bridging the gap between normal and dwarf ellipticals (the luminosity range between -18 and -20). As demonstrated in Schombert (2017), this gap is populated by the rare class of faint ellipticals with power-law surface brightness profiles, in the same structural family as normal ellipticals. The family of dE's have structurally distinct profiles from normal ellipticals, yet appear to transition coherently in color with normal ellipticals (Caldwell 1983).

This study will provide a detailed comparison of dwarf ellipticals with previous color studies and will also examine the differences between various photometric relationships. The colors presented herein will anchor the zeropoint of bright and dwarf elliptical colors for use by high-redshift studies. In addition, these colors will also provide a window into the stellar populations of ellipticals by comparison with simple and multi-metallicity population models where the wide wavelength coverage offers an avenue to break the age-metallicity degeneracy that plagues optical colors (Worthey 1994).

2. SAMPLE

The bright elliptical data for this study ($M_g < -20$) were based on the sample defined by Schombert & Smith (2012), a purely morphological sample of ellipticals selected from either the Revised Shapley-Ames (RSA, a catalog selected by luminosity) and Uppsala Galaxy Catalog (UGC, an angular limit catalog). The sample was restricted to large angular-sized ($D > 2$ arcmins) galaxies and required have been imaged by the *2MASS* project (we used J magnitudes as our baseline). In addition, the sample had to satisfy a criterion of isolation from foreground or background objects (i.e., there are no nearby bright stars or companion galaxies that would distort the surface brightness isophotes).

The resulting *JHK* surface photometry was presented in Schombert & Smith (2012), and the final sample consisted of 436 bright ellipticals. That sample was then cross-correlated with the *Galaxy Evolution Explorer* (*GALEX*, Martin *et al.* 2005), SDSS and *Spitzer* image libraries for existing data from 226.7nm (*GALEX NUV*) to $3.6\mu\text{m}$ (channel 1, *Spitzer*). Using automated scripts to browse the various mission websites resulted in 2,925 image files from the four missions. Overall there were 436 ellipticals in the *2MASS* sample, of which 149 had *GALEX* data, 252 had matching SDSS images and 149 with archived *Spitzer* $3.6\mu\text{m}$ images. These numbers are primarily determined by the varying sky completeness of

each mission.

In the original sample, only 5% of the galaxies were fainter than $M_g = -20$, which sharply degrades the ability to study the color-magnitude relation to low stellar masses. To extend the elliptical sequence, we have collected 60 more ellipticals from the recent early-type catalog of Dabringhausen & Fellhauer (2016, hereafter DF catalog) specifically for low absolute magnitude. Again, pure elliptical morphology and isolation were the requirement, plus the target had to be in the SDSS DR13 image library. In addition to these faint ellipticals (classed as E in the DF catalog), 62 dwarf ellipticals were also selected from the dwarf elliptical sample of Lisker, Grebel & Binggeli (2008) for study. Of this 62, 49 are classed dE(N), eight are classed dE(nN) and five as dE(bc) based on the Lisker scheme. A majority of these galaxies are in the Virgo cluster. The Virgo sample was combined with a sample of group dE from the DF catalog for a total dwarf sample of 62 galaxies. The combined sample (bright, faint and dwarf) contains 374 ellipticals with, at least, photometry from SDSS *ugri* images.

Each object in the total sample was also inspected for evidence of emission lines (excluding AGN features), dust or other signatures of recent star formation when spectroscopic data was available in the SDSS archive. The idea here was to find a sample of ellipticals that was as similar in terms of morphology and star formation history as possible. While some contamination of inner colors due to low level AGN activity was acceptable, their effects had to be restricted to inside the various mission's PSF or the galaxy was rejected from the sample. All the images were ellipse subtracted to look for asymmetric features that might be a signature of recent mergers or dust lanes. While the usual selection of boxy-like and disk-like residuals were observed, there were no obvious linear features. In addition, color subtracted frames were examined for an evidence of dust lanes, none were detected in the UV and optical images.

2.1. Data Reduction

Data reduction of the flattened, calibrated images from each mission was performed with the galaxy photometry package ARCHANGEL (Schombert 2011). These routines, mostly written in Python, have their origin back to disk galaxy photometry from the late 1980's and blend in with the GASP package from that era (Cawson 1987). The package has four core algorithms that 1) aggressively clean and mask images, 2) fit elliptical isophotes, 3) repair masked regions then perform elliptical aperture photometry and 4) determine aperture colors and asymptotic magnitudes from curves of growth and determine accurate errors based on image characteristics, such as the quality of the sky value.

The photometric analysis of galaxies branches into four areas; 1) isophotal analysis (the shape of the isophotes), 2) surface brightness determination and fitting (2D images reduced to 1D luminosity profiles), 3) aperture luminosities (typically using masked and repaired images and elliptical apertures) and 4) asymptotic or total magnitudes (using curves of growth guided by surface brightness data for the halos, see Schombert 2011). Ellipticals are the simplest galaxies to reduce from 2D images to 1D luminosity profiles since, to first order, they have uniformly elliptical shaped isophotes (Jedrzejewski 1987).

Where many ellipticals display disky or boxy isophotal shapes (Kormendy & Bender 1996), this deviation is at the few percent level and has a negligible effect on the surface brightness profile, aperture luminosities or colors values (Schombert 2013).

Surface brightness determination and fitting consumes a large fraction of the processing time for ellipticals. Accurate surface brightness profiles require detailed masking to remove foreground stars, background fainter galaxies and image artifacts. While cleaning an elliptical galaxy’s image is simplified by the lack of HII regions, dust lanes or other irregular features, the final accuracy of the profile will be highly dependent on the quality of the data image, in particular the flatness of the image and knowledge the true sky value. The smooth elliptical shape to early-type galaxies results in very low dispersions in intensity around each isophote that, in turn, makes the removal of stellar and small background galaxies an iterative task.

Following the prescription outlined in Schombert & Smith (2012), we processed all the mission images in the same manner. Despite the differing plate scales (i.e., arcsecs per pixel), orientations on the sky and flux calibrations, the *GALEX*, SDSS, *2MASS* and *Spitzer* missions all provide well flattened final data products, usually free of any obvious artifacts. Very little image preparation was required, other than confirming that the targets in the images were, in fact, the correct galaxy (galaxy misidentification in the archive servers was not uncommon). This was accomplished by comparison with the PSS-II J images at STScI/MAST and crude luminosity estimates compared to the RC3 magnitudes (de Vaucouleurs *et al.* 1991).

Isophotal fitting on each image begins with a quick visual inspection of the field for manual suppression of artifacts and marking the center of the galaxy. Then, an iterative ellipse fitting routine begins outside the core region, moving outward fitting the best least-squares ellipse to each radius until the isophote intensity drops below 1% of sky. The routine then returns to the core to finish the inner pixels in a like manner. During the ellipse fitting, pixels greater than (or less than) 3σ from the mean intensity are masked and removed using a 50% growth radius. The resulting fits are output as mean intensity, dispersion around the ellipse, major axis, eccentricity, position angle (and errors) plus the first four intensity moments. Conversion to surface brightness profiles uses the generalized radius, the square root of the major times minor axis (\sqrt{ab}). All spatial parameters will be quoted using the generalized radii.

Resulting elliptical isophotes are calibrated (intensity and pixel size) using the standard pipeline calibrations provided by the missions, then processed into surface brightness profiles. Various fitting functions have been applied to elliptical surface brightness profiles over the years. A full discussion of their various strengths and weaknesses can be found in Schombert (2013). In brief, the Sérsic $r^{1/n}$ provide the best fits over the full range of surface brightness, but suffers from coupling between its shape and characteristic radii parameters that reduce its usefulness. Templates are stronger match to the shape of elliptical profiles (Schombert 2015), but are only parametrized by luminosity and do not provide any

structural metrics. In the end, we found that empirically determined parameters, such as half-light radius (r_h) and mean surface brightness ($\langle \mu \rangle$), are the most strongly correlated parameters with luminosity or stellar mass.

As this study is primarily concerned with colors, the determination of luminosity in a consistent and accurate manner from the datasets is of the highest priority. Aperture luminosities are calculated using the ellipses determined by the isophote routines. Care was taken to make sure that the same eccentricities and position angles were used across the various mission images. None of the sample galaxies display any variation in eccentricity or position angle at the 2% level from the near-UV to the far-IR. Thus, aperture values were, in effect, determined using fixed radii in kpcs.

The total luminosity of a galaxy is a much more problematic value to determine. The procedure used here is outlined in Schombert (2011), where elliptical apertures are determined by a partial pixel routine from the masked images where the masked regions have been filled by the local mean isophote. While it seems obvious that masked regions would reduce the calculated flux inside an aperture, in fact, this effect is rarely more than 5 to 10% the total flux of an elliptical. However, this effect is also unlike Poisson noise in that it always works to reduce the measured luminosity. The cleaned images are then integrated as a function of radius to produce curves of growth. An added feature is that as the outer aperture are integrated, their fluxes are corrected by the mean isophotal intensity as given by either the raw surface brightness profile or the Sérsic $r^{1/n}$ fit to the profile. This reduces the noise in the outer apertures and often produces a smoother convergence to a stable total flux.

The half-light luminosity, and radius, used in our bright elliptical sample, was found to be unstable for the dwarf ellipticals. Their smaller angular size and exponential profiles introduce unacceptable error in the determination of the half-light radius. Instead, for this paper, we have used the Holmberg radius which is the radius where the g surface brightness profile reaches $25 \text{ mag arcsec}^{-2}$. The Holmberg luminosity is the aperture luminosity calculated inside this radius and, typically, results in 92% of total of the total luminosity (although this varies slightly with filter choice, Schombert 2016). While this choice has little impact on measured colors (color gradients are the dominate source of color variation), for relationships that compare total luminosity (a proxy for total stellar mass) with color (e.g., the CMR) then the aperture luminosity is corrected for the missing 8% to bring the luminosities in alignment with the half-light values from Schombert (2016).

In a majority of the missions, the error quoted at the archives for the total and aperture magnitudes severely underestimates the actual error found in this study (see Schombert 2016, §2.2, 2.3, 2.4 and 2.5). This is due to the fact that their error calculations focus, primarily, on the Poisson noise that is proportional to device sensitivity and exposure time. However, for large extended sources ($D > 2 \text{ arcmins}$) or ones that are low in mean surface brightness (i.e., dwarfs), the primary source of noise is uncertainty in the sky value and the variation of sky across the image. Sky for this study was determined by two separate algorithms. The first is the manual sec-

tion of between 10 and 20 sky boxes (typically 20 by 20 pixels in size) in regions surrounding the target (outside its halo), but separate from other galaxies or bright star halos. The dispersion of the mean from averages in each sky box provide the best value for the uncertainty on the sky value (Schombert 2013). Total errors quoted in this paper are then calculated as 3σ from the mean sky value applied to the sum of the pixels in each aperture. As a check to the correct sky value, the elliptical isophotes are fixed in shape and tabulated beyond the galaxy radius to the edge of the frames. These outer ellipse intensity values should converge on the sky value determined from the sky boxes. In the few cases where the two values disagree, the ellipse sky value was used, but the error estimates continued to use the dispersion between the sky boxes.

Full surface brightness analysis is performed on all the filter images. Thus, a second determination of color is possible by examining color as measured by the difference in the surface brightness profiles directly. While any particular color surface brightness isophote contains much more error than the comparable aperture color at the same radius, at large radii this method can be more informative as the number of pixels used is large compared to the sky error. Of course, color gradients are the primary use for multi-filter surface brightness profiles. And, again, with the regularity of shape for ellipticals, the run of color with radius is a direct measure of the projected 2D distribution of stellar populations. The best measure of the core color of an elliptical is the interpolation of the color surface brightness profiles to zero radius.

Apparent uncorrected luminosities are designated by lowercase letters (e.g., m_{NUV} for raw *GALEX* *NUV* luminosities). Absolute luminosities, radii and colors are corrected for Galactic extinction following the prescription of Cardelli, Clayton & Mathis (1989) and $E(B - V)$ values from NED. Magnitude units varied between the missions; *GALEX*, SDSS and *WISE* use the AB/Vega system (*NUV*, *u*, *g*, *r*, *i*, *W1*, 3.6) and *2MASS* used the Johnson system (*J*, *H*, *K*). We have noted in our discussions when the various units are used. Distances used are the 3K CMB distances using the Benchmark model values for the standard cosmological constants (in particular, $H_o = 75$ km/sec/Mpc). A majority of the dE's were located in the Virgo cluster and a distance modulus of 31.09 was assumed. As none of the galaxies in this sample have redshifts greater than 0.04, no k-corrections were applied to the data. The final data products are too extensive to be listed in this publication. Instead, the author maintains all the data, reduction scripts and log files at his website (<http://abyss.uoregon.edu/~js>). We follow the philosophy of presenting all the reduction techniques as user enabled scripts, rather than a detailed description of the various steps leading from raw images to final luminosities and colors.

2.2. True Internal Colors

One point about galaxy colors that is often unspoken, and assumed to be known to the reader, is that a color quoted for a particular region in a galaxy does not represent the color of the stellar population at that 3D coordinate, but rather a pencil beam average of the stellar population colors between the observer and infinity.

Thus, the measured color at a particular elliptical annulus traced by an elliptical fit of radius, r_o , is, in fact, the luminosity weighted sum of colors of all the isophotes at radii $r > r_o$. This effect will be greater for small radii, where the pencil beam crosses through all the isophotes in the galaxy profile, and less for outer radii, where the pencil beam passes through a fewer number of isophotes with colors similar to the starting radii (for typical color gradients). Negative color gradients (decreasing color with radius) will result in underestimating the true color of a position with more significance for stronger gradients and steeper profiles.

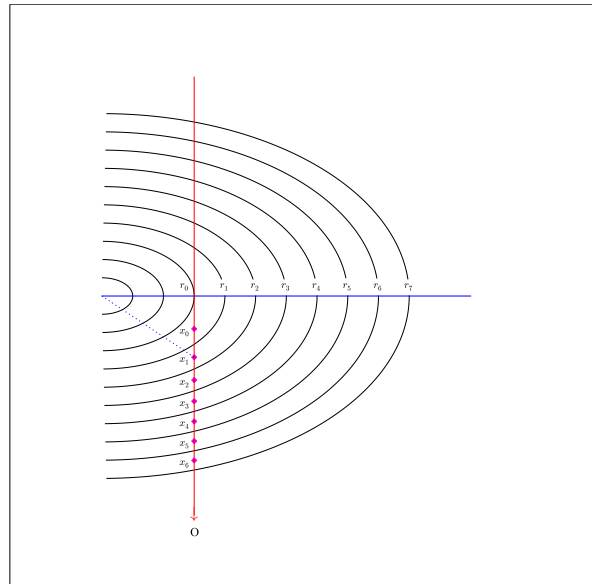


FIG. 1.— Calculation of the true color of a 3D section of an elliptical. Any measurement of a color value at a projected radius (r) is, in fact, the sum of the color intensities through a cross section (red line) toward the observer (O). Two factors determine the observed color, the surface profile of the galaxies and the color gradient. With both decreasing surface brightness and color, the true color at radius r_n is the sum of the intensity weighted colors at x_n . Knowledge of the surface brightness profile and color gradient allow an iterative procedure to deduce the true color at r_n .

Some information on this effect can be extracted if the run of surface brightness and color with radius is known. For example, one can bootstrap backwards for each position, iterating on cells of luminosity perpendicular to the surface brightness profile using the annulus luminosity density as an estimate of the cells in the pencil beam (see Figure 1). Then the colors from the radial gradient are assigned to each cell, weighted by cell size and luminosity then summed. This value is compared to the integrated color for that radius and iterated until they agree. The resulting color of the inner cell represents the true internal color at that radius, in particular, the extrapolation to the galaxy center then represents the true color at the core. The calculations depend on the assumed 3D shape that the pencil beam is passing through. However, numerically, this is only a 5% correction for extreme prolate or oblate shapes that is typically much less than the outer color errors and this correction decreases toward the center.

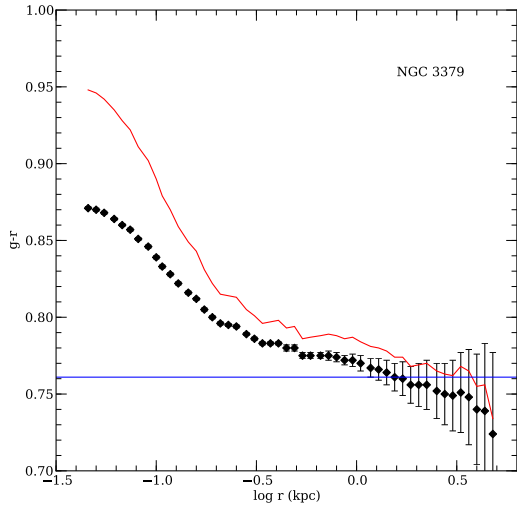


FIG. 2.— The run of true color with radius for NGC 3379, an intermediate luminosity elliptical. The observed color gradient (in $g-r$) is shown as the black symbols and errorbars. The deduced true $g-r$ colors as a function of radius are shown as the red line. With the typical blue color gradients in ellipticals, the true color gradient will always be redder than the observed as the line-of-sight passes through the bluer halo to reach the actual stellar region at radius r . The mean color of the galaxy is shown as the blue line.

An example of this effect on the impact for color gradients is shown in Figure 2. The raw color gradient is shown as black data points with the true internal corrected colors as the red line. The blue line is the total color of the galaxy from elliptical apertures. Note the total color is lower than the mean color from the surface photometry due to the negative color gradient producing bluer colors in the outer isophotes that contain more integrated flux than the inner core pixels. The true color is typically 0.01 to 0.02 redder for intermediate radii, but rises to 0.08 redder in $g-r$ in the central regions. A true core color will be significantly redder (or bluer depending on slope of the color gradient) than a total or halo color. This will be considered in the discussion section (see S3.3).

2.3. WISE

Differing from the photometry of normal ellipticals in Schombert (2016), we have added archive data from the *WISE* mission to the whole dataset, mostly to offset the lack of *2MASS* photometry for the dE’s in the sample due to the surveys low limiting magnitude. The *WISE* MIDEX mission (Wright *et al.* 2010) was a cryogenically-cooled 40 cm telescope equipped with a camera containing four mid-infrared focal plane array detectors that simultaneously imaged the same 47×47 arcmin field-of-view. The entire sky was imaged at 3.4, 4.6, 12 and $22 \mu\text{m}$ (labeled as *W1*, *W2*, *W3* and *W4* filters) using a HgCdTe 1024×1024 array with 2.76 arcsecs per pixel plate scale for the *W1* filter. Processed images, obtained from IRSA, are flattened, sky-subtracted, calibrated frames with plate scales of 1.375 arcsecs per pixel and resolution of 8.5 arcsec PSF. The PSF is poor, compared to our

other datasets, but adequate to obtain Holmberg magnitudes and colors.

The dwarf ellipticals in this sample were all too faint to be detected in *2MASS* *K* images, and very few were targeted by *Spitzer*. Thus, comparison to the bright elliptical sample was problematic in the near-IR. Instead, the *WISE* archive was searched for the dE’s in our samples with *GALEX* and *SDSS* coverage (as well as the bright and faint elliptical samples). In total, 60 dE’s from the DF catalog met these criteria and have a full range of wavelength coverage. All the ellipticals in the bright (252) and faint (60) samples had *WISE* coverage. Figure 3 displays two colors that cover all three major datasets (*GALEX* *NUV*, *SDSS* *ugri* and *WISE* *W1*) and for the three components of our sample (bright ellipticals at $M_g < -20$, faint ellipticals between $-20 > M_g > -16$ and the dwarf ellipticals selected by morphology). The dispersion is not due to photometric errors, rather the well-known color-magnitude relation, that is more evident at long wavelengths than short (Bouquin *et al.* 2015). The dwarf ellipticals notably distinguish themselves in visual appearance, surface brightness profile shape and color.

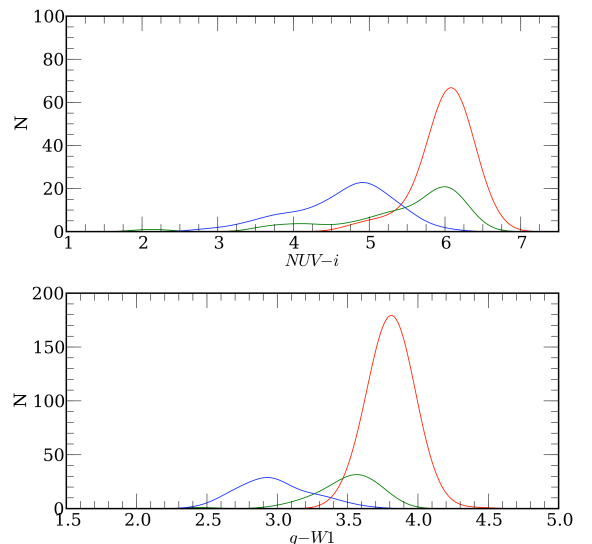


FIG. 3.— Normalized histograms for the sample through two colors, $NUV-i$ and $g-W1$. The bright elliptical sample (252 galaxies, $M_g < -20$) is shown in red, the faint elliptical sample (60 galaxies, $-20 > M_g > -16$) in green and the dwarf ellipticals in blue. The color-magnitude effect is evident, although the dwarf sample, selected by morphology, still distinguishes itself by color as well. Notice, the range in $g-W1$ color is similar to canonical values in $V-K$, as the two color map linearly into each other.

It is worth exploring the behavior of the three near-IR filters from *2MASS*, *WISE* and *Spitzer* (*K*, *W1* and $3.6 \mu\text{m}$) since most SED models produce *K* colors and, hopefully, can be easily converted to *W1* or $3.6 \mu\text{m}$. These filters have wavelength centers at $2.16 \mu\text{m}$ (*2MASS* K_s), $3.35 \mu\text{m}$ (*WISE* *W1*) and $3.55 \mu\text{m}$ (*Spitzer* 3.6) respectively. The bandwidths are $0.26 \mu\text{m}$, $0.66 \mu\text{m}$ and $0.75 \mu\text{m}$, where *2MASS* *K* is in the Johnson system and *W1* and $3.6 \mu\text{m}$ are in the AB magnitude system. The sample of ellipticals with *K*, *W1* and $3.6 \mu\text{m}$ observations were culled from the main sample. There were 253 ellipticals

TABLE 1
MEAN NEAR-IR COLORS

| M_g | $K - W1$ | N | $W1 - 3.6$ | N | $K - 3.6$ | N |
|---------|-------------------|-----|-------------------|----|-------------------|----|
| < -21 | 0.075 ± 0.067 | 160 | 0.089 ± 0.028 | 39 | 0.177 ± 0.074 | 42 |
| > -21 | 0.059 ± 0.077 | 93 | 0.081 ± 0.072 | 41 | 0.148 ± 0.056 | 40 |
| total | 0.070 ± 0.073 | 253 | 0.086 ± 0.029 | 80 | 0.162 ± 0.066 | 82 |

with $K - W1$ colors, 80 ellipticals with $W1 - 3.6$ colors. The sample was taken as a whole and mean colors were deduced using a jackknife average. Then the sample was divided into two subsets at the midpoint in luminosity, one brighter than $M_g = -21$, the other fainter. The resulting values, plus dispersions are listed in Table 1.

The small change in the near-IR colors is unsurprising given that each filter is close to each other in central wavelength, plus the SED of an old stellar population peaks around $3\mu\text{m}$ and each filter is basically sampling a flat portion of a galaxy’s SED with little dependence on the metallicity of the galaxies. There is a slight change in color with absolute luminosity for $K - W1$ and $K - 3.6$ (0.016 and 0.019 respectfully), but this change is barely significant and formal fits to the near-IR CMR produces a correlation coefficient of less than 0.15.

There is also very little evidence of a color term in the two color diagrams where either $K - W1$, $W1 - 3.6$ and $K - 3.6$ are one axis. For example, in $u - i$ versus the near-IR colors there is a range from 2.0 to 3.4 in $u - i$, but mean $K - W1$ color only varies from 0.055 to 0.070 with a dispersion of 0.085. Any color variation is minor compared to the internal errors on the aperture colors. With respect to correcting the K magnitudes and colors from SED models to $W1$, we have adopted a $K - W1$ color of 0.070 with the caveat that for the bluest dwarf ellipticals an addition correction of 0.010 could be applied and limits the interpretation of age and metallicity by that amount.

3. DISCUSSION

The analysis of the colors of dwarf ellipticals follows the procedure outlined in Schombert (2016) for bright ellipticals; the empirical two-color relationships for all the optical and near-IR filters, comparison to multi-metallicity population models and the color-magnitude relation. For clarity, we divide the discussion of the two-color relations into those defined by filters close in wavelength (near colors) and those whose filters are widely separated in wavelength (far colors).

3.1. Near Colors

The colors of the new faint and dwarf ellipticals in our sample extend the relations found in Schombert (2016) by six more magnitudes in luminosity. The near colors are defined by the near-UV and optical filters (*GALEX* *NUV*, *SDSS* *ugri*). Four of these two-color relations, between neighbor filters, are shown in Figure 4 along with MW and M31 globular cluster colors from Galleti *et al.* (2009) and Peacock *et al.* (2010). The mean error bars for each of the samples is also shown. In general, the colors are coherent from each of the samples, meaning that galaxies that are blue (or red) in one color set

are also blue (or red) in other filter combinations. The exception are *NUV* colors that display a turnover at the reddest colors. As discussed in Schombert (2016), this behavior is well modeled by the single abundance scenario proposed by Yi *et al.* (1998) and underlies the importance of a small metal-poor population to colors even in massive ellipticals dominated by metal-rich stars (see Rakos *et al.* 2008).

Also shown for the SDSS colors (u, g, r, i) are stellar population models for 12 and 5 Gyrs for varying mean metallicities. Again, as discussed in Schombert (2016), the bluer colors ($u - g$ vs $g - r$) indicate that an internal metallicity distribution is required to match the global colors (so-called multi-metallicity models, Schombert & Rakos 2009). Where the bluer $u - g$ colors are influenced by a small metal-poor population (also seen in the *NUV* colors), presumably a population of between 5 to 10% of the total stellar mass that is composed of the first generation of stars with near globular cluster metallicities. The multi-metallicity models (shown in Schombert 2016) follow the bright ellipticals colors to a greater degree than single metallicity models (SSP, see Schombert 2016).

The SDSS colors display the well-known degeneracy between age and metallicity. The 12 and 5 Gyr SSP tracks are indistinguishable in two-color space, although the 5 Gyr models require extremely high metallicities ($[\text{Fe}/\text{H}] > 0.6$) to match the colors of the brightest ellipticals. In a single two-color comparison, it is impossible to separate the possibility of very young stellar populations with high metallicities versus older stellar populations with low metallicities. Separation can be achieved with a longer wavelength baseline in color due to the fact that age and metallicity, while still coupled at all optical and near-IR colors, have varying contributions to color as one goes to longer wavelengths (see §3.3).

As noted by Schombert (2016), the trend for positively correlated colors is seen in all colors except for $NUV - u$. Elliptical colors are, in general, coherent from filter to filter (i.e., red galaxies are red in all filters). In addition, outliers are usually outliers across all their colors with the probable explanation that some contamination is in the galaxy itself or undetected strong emission lines or simply a flaw in the calibration and/or reduction pipeline. Their rarity did not warrant extensive investigation as they are not relevant to the averaged results. Correlations between colors have the lowest scatter for widely spaced filters, mostly because filters close in wavelength have less dynamic range (the slope of the galaxy SED varies little over small changes in wavelength except near the 4000Å break) and photometric errors play an increasing role.

A criterion for recent star formation in bright ellipticals was a $NUV - r$ cutoff at 5.5 (Schawinski *et al.* 2007) of which 93% obey this selection. However, for luminosities fainter than -20 , only 40% had redder colors and, for the dE sample, only 3% have redder colors. This probably does not reflect a steep increase in recent SF for lower mass ellipticals but, rather, is the effect of decreasing metallicity where colors bluer than $NUV - r = 5.5$ are typical for old stellar populations with mean $[\text{Fe}/\text{H}] < -0.5$ (Schombert 2016). Younger mean age is not ruled out in dE’s based solely on *NUV* colors, however, UV colors, by themselves, can not conclusively demon-

strate younger age. The locus of late-type RC3 galaxies is shown in the upper right panel of Figure 4. At the blue end of this sequence are galaxies with current star formation rates between 0.10 and 1 M_{\odot} per yr. Only a handful of dE’s approach this color realm.

With respect to the three ellipticals groups (bright, faint and dwarf), the trend for bluer colors in all filters is evident. Where the bright ellipticals defined an extrapolation of the globular cluster colors in all filters, the faint ellipticals clearly overlap with the reddest globulars and the dwarf ellipticals are consistent with the mean globular clusters leaving only the most metal-poor globulars at the extreme end in color. If color maps directly into $[\text{Fe}/\text{H}]$ (which it probably does not for the dE’s, see §3.4), then the faint ellipticals have $[\text{Fe}/\text{H}]$ values slightly less than solar and dE’s range from -1.5 to -0.5 in average metallicity. This is consistent with the CMR (see §3.3).

There is some tendency for the dwarf ellipticals to be slightly bluer, on average, than the globulars in the bluest colors ($NUV - g$ and $u - g$). However, they are in agreement for the redder colors ($g - r$ and $r - i$). Any deduction of $[\text{Fe}/\text{H}]$ from colors, as in Schombert (2016), assumes a 12 Gyrs age and agreement across the optical and near-IR colors with the bright ellipticals whose metallicity calibration is set by the globular cluster two-color relations. We will explore this discrepancy as it impacts their estimate of mean age and metallicity for dE’s in §3.4.

We also note the recently published SDSS and K colors for a broad sample of Virgo globular clusters (Powalka *et al.* 2016) is shown in Figure 4 as a magenta line. This line represents a moving average in color space of 1850 globulars. The trend in two-color space is identical to MW and M31 globulars, although there is a tendency to slightly redder blue colors at the high metallicity end of the Virgo globulars sequence. Whether this signals a break in the age-metallicity relation for globulars in Virgo, compared to the Milky Way and M31, or a shift in the color calibration at redder colors is unclear. We will continue to use the MW/M31 sequence to define the 12 Gyrs locus and calibration of $[\text{Fe}/\text{H}]$ for ellipticals as outlined in Schombert (2016).

3.2. Far Colors

The similarity between normal and dwarf ellipticals, and globular clusters, continues in the colors with the largest wavelength separation shown in Figure 5. Here, the *WISE* filter $W1$ replaces the *2MASS* K filter from Schombert (2016) with only a nominal correction to stellar population models to jump from K colors to $W1$ colors. Again, the trends from Schombert (2016) are reproduced, now with a greater range of galaxy luminosities (i.e. bluer colors). The optical to near-IR colors display high uniformity from bright to dwarf ellipticals. This would rule out a strong AGB contribution for dwarf ellipticals compared to normal ellipticals as this would be signaled in a sharp change in slope in optical to near-IR two-color diagrams (see Schombert & McGaugh 2014). A lack of AGB colors, in turn, rules out an strong star formation in the last few Gyrs.

As with the near colors in Figure 4, the far colors also display the behavior of the dwarf ellipticals overlapping with the intermediate metallicity globular clusters ($[\text{Fe}/\text{H}]$ between -1.5 and -0.5). SSP models for the far

colors have very little separation by age, tracking parallel to color-color sequences with only metallicity to provide the sole variation in color. Thus, these individual colors, by themselves do not distinguish between a subsolar dE population of 12 Gyrs or a near solar metallicity dE population, but with ages less than a Gyr.

However, there is a subtle change as one goes from $u - W1$ to $i - W1$. While the bright and faint normal ellipticals maintain their relative distributions with respect to globular cluster colors, the dwarf ellipticals become increasingly redder with respect to the mean globular color. This can be seen by using the mean color of the globular clusters and bright ellipticals as an anchor to the reddest and bluest colors from u to $W1$. The mean color of the faint elliptical sample lies at 0.71, 0.69, 0.69 and 0.68 in the fraction of this interval for $u - W1$, $g - W1$, $r - W1$ and $i - W1$. On the other hand, the mean dE sample color lies at 0.26, 0.19, 0.16 and 0.12 for the same colors and interval. In other words, the mean color for dE’s decreases, with respect to normal ellipticals, as we go from $u - W1$ to $i - W1$.

This behavior is unexpected since the color of normal ellipticals with respect to the globular clusters was extremely consistent from *GALEX* to *Spitzer* (Schombert 2016). In fact, assigning a metallicity value, just from a normal ellipticals color using globulars as a calibration, produced a consistent and robust measure even if the scatter in an individual color was high. This procedure will fail for dwarf ellipticals as using colors closer in wavelength will result in increasing low $[\text{Fe}/\text{H}]$ values. The most obvious explanation for this type of color behavior is an age effect, that was first indicated with narrow band colors (Rakos & Schombert 2004) and will be discussed in §3.4.

3.3. Color-Magnitude Relation

It was demonstrated in Schombert (2016) that the CMR is primarily a relationship between stellar luminosity (a proxy for total galaxy stellar mass) and mean metallicity. While limited age and recent star formation effects can not be completely excluded (e.g., Faber *et al.* 1995), these effects are at the 5% level for colors (although may have a larger contribution for spectral indices studies). The slopes for the CMR, found in Table 3 of Schombert (2016), are identical to slopes from other CMR studies (Bernardi *et al.* 2003, Chang *et al.* 2006). Changes in the slope of the CMR with redshift is an interesting measure of galaxy chemical evolution, so the accurate slope values for zero redshift samples is an important parameter.

The CMR for near and far colors are shown in Figures 6 and 7. There is no evidence that the new sample of faint ellipticals deviates from the CMR slopes fit to the bright ellipticals (shown in each Figure as green symbols). This makes a solid statement that *power-law shaped ellipticals, that define the bright and faint ellipticals sample (Schombert 2017), also obey the same structural and stellar population relationships*. This will be somewhat of a challenge to many hierarchical models of galaxy formation which predict extended epochs of star formation that varies significantly with mass (Naab *et al.* 2007). However, age determination with colors allows for a great deal of flexibility with respect to the first epoch of star formation and its initial duration (for example,

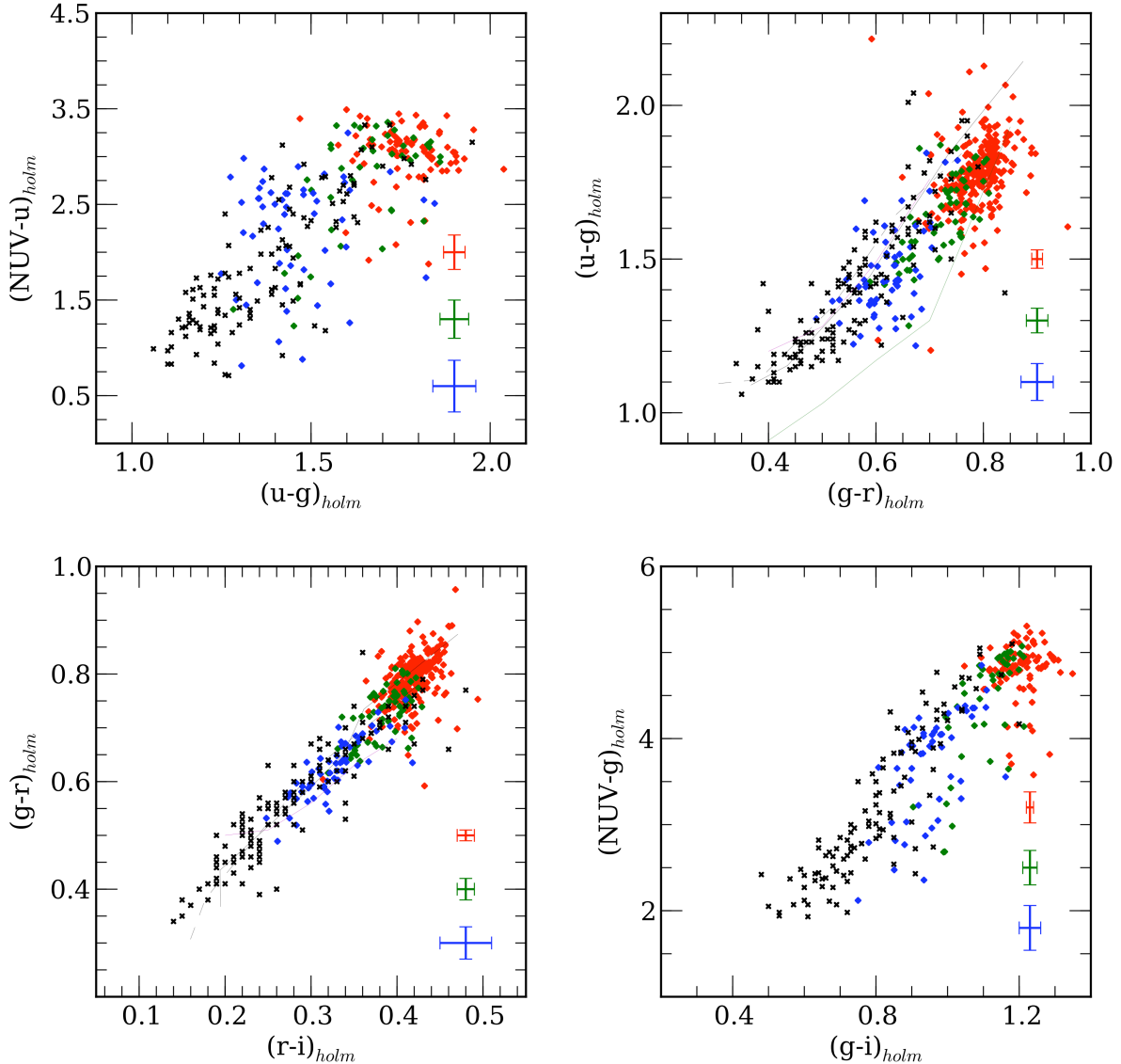


FIG. 4.— The two-color relations for *GALEX* and *SDSS* near colors ($NUV - u$, $u - g$, $g - r$, $r - i$). Red symbols are bright ellipticals ($M_g < -20$), green symbols are faint ellipticals ($M_g > -20$), blue symbols are dwarf ellipticals (dE) and black crosses are M31 and MW globular clusters. All colors are based on Holmberg aperture luminosity values (the Holmberg radius determined in the g frames and applied to the other filters). Typical error bars as shown on the right side of every panel. The solid black line is a 12 Gyrs SSP model, the dashed line is a 5 Gyrs model (varying from $[Fe/H] = -2.5$ to $+0.3$). The magenta line is the average colors 1850 globulars in the Virgo cluster (Powalka *et al.* 2016). The green line is the locus of RC3 Sb-Sm galaxies, i.e. a locus of star-forming colors.

a shorter duration at a later epoch will mimic a long duration SF event at early epochs, see below).

There is no evidence in any color combination that normal ellipticals are composed of a significant stellar population with ages less than 12 Gyrs (Rakos, Odell & Schombert 2008, Schombert 2016, although see a dissenting view in Graves, Faber & Schiavon 2010). And, thus, the slopes of the various CMR’s are consistent, across all the wavelengths, with a pure metallicity interpretation in a generally old stellar population. Even small variations in mean age (greater than 4 Gyrs) would result in different slopes between blue and near-IR colors (if age varied with stellar mass, see Eigenthaler & Zeilinger 2013; Smith *et al.* 2012). As demonstrated in Schombert (2016), there is no indication of an age effect in the CMR, and the new sample of fainter ellipticals supports this

conclusion. This implies that the CMR is, in fact, purely a metallicity relationship, presumably between the stellar mass that produces metals and, later, produces the galactic winds that remove the remaining gas and halt star formation and chemical enrichment (see Matteucci 2007).

The identical CMR slopes for bright and faint ellipticals implies that we can use the same techniques of assigning a mean metallicity to the new, low luminosity sample as we did the brighter ellipticals in Schombert (2016). As outlined in Schombert (2016), each color can be assigned a metallicity-color relation as guided by the predictions from multi-metallicity population models (Schombert & Rakos 2009) tied to the globular cluster $[Fe/H]$ values. A guide to the accuracy of this method is to compare the spread in $[Fe/H]$ as deduced from col-

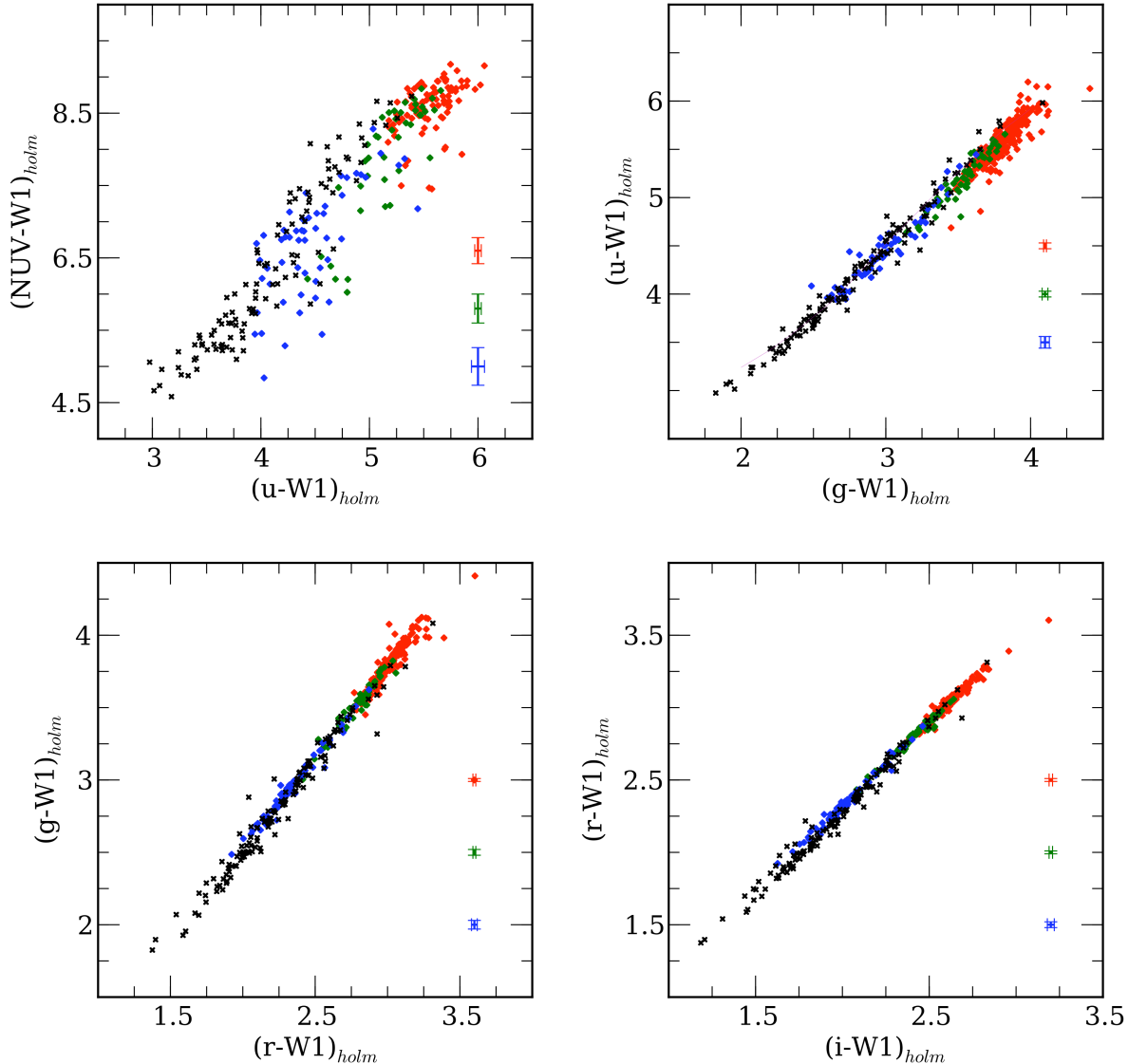


FIG. 5.— The two-color relations for *GALEX*, *SDSS* and *WISE* far colors ($NUV - W1$, $u - W1$, $g - W1$, $r - W1$, $i - W1$). Red symbols are bright ellipticals ($M_g < -20$), green symbols are faint ellipticals ($M_g > -20$), blue symbols are dwarf ellipticals (dE) and black crosses are M31 and MW globular clusters. All colors are based on Holmberg aperture luminosity values (the Holmberg radius determined in the g frames and applied to the other filters). Typical error bars as shown on the right side of every panel. The solid black line is a 12 Gyrs SSP model, the dashed line is a 5 Gyrs model (varying from $[\text{Fe}/\text{H}] = -2.5$ to $+0.3$). The magenta line is the average colors 1850 globulars in the Virgo cluster (Powalka *et al.* 2016).

ors. This technique produced a mean dispersion of 0.15 dex in metallicity for both the bright and faint elliptical samples. Mapped onto the CMR, this results in $[\text{Fe}/\text{H}]$ values of 0.5 for the brightest ellipticals decreasing to -0.2 for ellipticals around -19 .

The behavior of the colors for dwarf ellipticals differs from the normal ellipticals in that a majority (varying between 60 and 80%) have colors bluer than expected for their luminosities based on a linear extrapolation of the CMR. Small number statistics make it impossible to determine if the dwarf ellipticals form their own sequence or are a non-linear extension to the normal elliptical sequence. We can only state that the brightest dwarf ellipticals have colors near the CMR and the deviation becomes greater at lower luminosities. And, while most the dE's in the sample have colors that place them below an extrapolation of the CMR from normal ellipticals, that

deviation is greatest at the longest wavelengths. From the near-IR colors there is a clear indication that the dwarf ellipticals deviate from the normal elliptical to a greater extent with decreasing luminosity than is seen in the optical colors.

If one assumes that metallicity is still the primary driver for the CMR in dwarf ellipticals and one applies the same metallicity-color relations for normal ellipticals to dwarf ellipticals, then the CMR for dE's implies $[\text{Fe}/\text{H}]$ values near -0.2 for the brightest dE's decreasing to -1.0 for the faintest dE's in our sample. However, this is not consistent between the colors. For example, the u and $W1$ colors derive $[\text{Fe}/\text{H}]$ values near -1.5 for the faintest dE's while the gri colors derive much higher values near -0.5 for the same galaxies. This type of behavior, not found in normal ellipticals suggests another parameter, the most obvious being age is in play (although one could

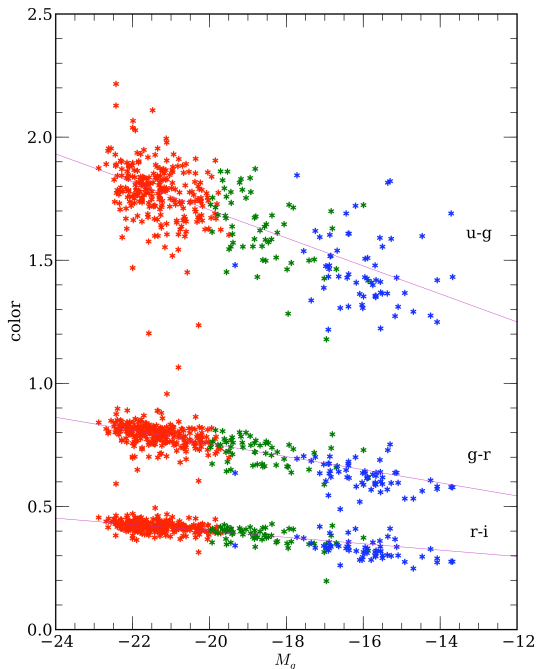


FIG. 6.— The CMR for near optical colors. Red symbols are bright ellipticals $M_g < -20$ with power-law shaped profiles. Green symbols are faint ellipticals ($M_g > -20$) with power-law shaped profiles. Blue symbols are dwarf ellipticals by morphology. The bright and faint ellipticals follow the same linear fit (slope and zeropoint). While the dE’s are slightly bluer in $g-r$ and $r-i$ from the normal elliptical fit (e.g., 80% of the dE’s are below the fit in $r-i$. The deviation becomes more prominent at redder colors.

entertain extreme IMF and extinction values).

3.4. Younger Age for Dwarf Ellipticals

It is possible to estimate the magnitude of an age effect on the complete sample of dwarf ellipticals, without assigning a specific age to each galaxy. The technique follows the prescription outlined in Schombert (2016) with respect to bright ellipticals. A metallicity can be assigned to each color combination based on a procedure of taking SSP models and convolving them to a multi-metallicity framework (one that assumes an underlying metallicity distribution based on high resolution studies of nearby ellipticals, see Monachesi *et al.* 2011). The zeropoint to these multi-metallicity models is set by globular cluster colors (both MW and M31 samples) whose mean $[\text{Fe}/\text{H}]$ values are determined directly from their CMD’s. As discussed in Schombert (2016), single population models are a poor description of bright elliptical colors, whereas multi-metallicity predictions reproduce the mean colors and CMR of bright ellipticals without any need to introduce a younger component to a pure 12 Gyrs population.

Using these color to metallicity models, and assuming a 12 Gyrs age, each color predicts a $[\text{Fe}/\text{H}]$ value. Any systematic deviations from a mean $[\text{Fe}/\text{H}]$ based on an average of all the colors would signal a problem for the technique, such as a 2nd parameter other than metallicity (e.g., age or IMF variations) as the main determinant in the continuum shape of galaxy spectra (i.e., colors). None were seen in the faint plus bright elliptical samples and the scatter in the deduced $[\text{Fe}/\text{H}]$ values were solely owing to error in the colors.

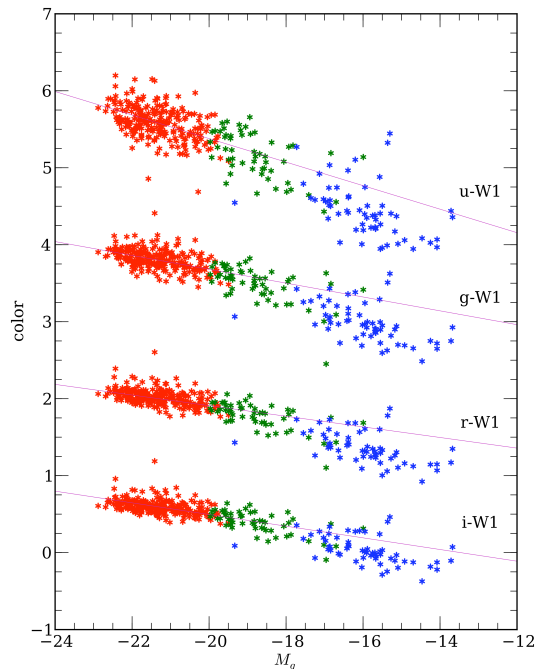


FIG. 7.— The CMR for far color, optical to near-IR. Symbol colors are the same as Figure 6. The deviation of dwarf ellipticals from the normal elliptical CMR is more obvious in the near-IR colors. The sequence from bright to fainter dE’s deviates farther from the normal elliptical fit with decreasing luminosity. However, even a majority of brightest dwarf ellipticals are below the normal ellipticals CMR.

We can now apply those metallicity calibrations to the dwarf elliptical colors, again with the assumption of a solely metallicity driven continuum and a mean age of 12 Gyrs. As expected from the deviations in the CMR, this procedure fails. The colors for faint ellipticals are in line with the bright ellipticals (see Figure 8), and even the brightest dE’s are consistent from color to color. But a majority of the dE’s do not produce consistent $[\text{Fe}/\text{H}]$ values. Typically, they overestimate $[\text{Fe}/\text{H}]$ for blue colors and underestimate $[\text{Fe}/\text{H}]$ for red and near-IR colors. One such color combination is shown in Figure 8 for the metallicity deduced from $g-r$ versus the metallicity deduced from $g-W1$. The normal ellipticals display a good one-to-one correspondence between the calculated $[\text{Fe}/\text{H}]$ values. However, the dwarf ellipticals begin to deviate below metallicities of -0.3 and a majority have near-IR calculated $[\text{Fe}/\text{H}]$ values 0.5 dex below those calculated from optical colors.

If one relaxes the age requirement of 12 Gyrs, for example assuming a mean age of 5 Gyrs, then the one gets the resulting metallicity track as shown in Figure 8 (green dotted track). The deviation in color is well matched to an age effect, but now the deduced $[\text{Fe}/\text{H}]$ values become non-unique as there is a wide range of possible age and metallicity combinations that produce the observed colors. Some of this range can be narrowed by using multi-age tracks across several color combinations. The result of this numerical experiment is such that dwarf ellipticals seem to range in age from 12 to 6 Gyrs in age, and -0.3 and -1.4 in $[\text{Fe}/\text{H}]$. There is a clear trend of decreasing metallicity and decreasing age with luminosity (stellar mass). The positions of the Local Group and Fornax

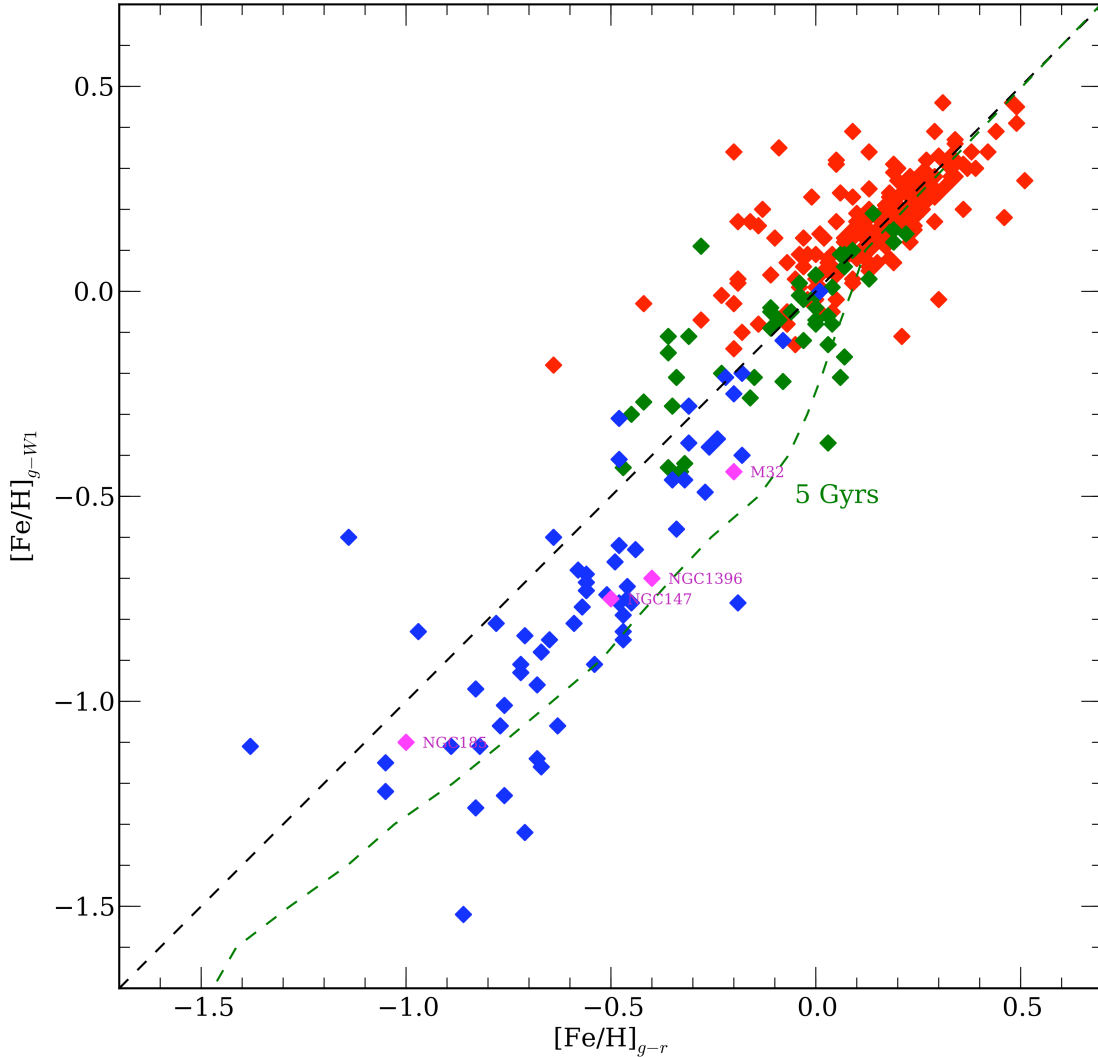


FIG. 8.— An example of $[\text{Fe}/\text{H}]$ deduced from colors, calibrated to the MW/M31 globular cluster metallicities (Schombert 2016). Bright and faint ellipticals produce coherent $[\text{Fe}/\text{H}]$ values from color to color ($\sigma = +0.15$ dex). However, the dwarf elliptical sample deviates from the unity line in a systematic fashion which indicates an age effect. A 5 Gyrs model is placed in the same color-color space which deviates downward for metallicities deduced from near-IR colors. dE’s range from 2 to 8 Gyrs younger than normal ellipticals, with mean age decreasing with decreasing dwarf mass. Also the positions for three dE’s in the Local Group (M32, NGC147 and NGC185) plus one Fornax dE (NGC1396) are indicated using their CMD determined age and metallicities with respect to the models.

dE’s, with CMD determined ages and metallicities, are indicated using the model predictions. Their positions agree well with the general trend of the dE sample.

4. CONCLUSIONS

A difference between the CMR for normal and dwarf ellipticals can be traced back to Caldwell (1983). His Figure 3 displays the $U - V$ colors for a small sample of Virgo bright ellipticals plus a sample of 19 dE’s. While the bright end of the CMR is ill-defined, the dwarf ellipticals clearly lie blueward of a linear extrapolation of the bright elliptical trend. Interpretation at that time focused on recent star formation in dwarf ellipticals, but concluded that massive stars were missing and the bluer colors were due to a younger mean age.

Some curvature in the optical CMR, at high and low luminosities, was detected by Bernardi *et al.* (2011). They covered a range of -18 to -24 in SDSS r , compared to our study from -15 to -24 . We do not, statistically, de-

tect an upturn at high luminosities in our sample, but the amount they claim is within our errors. An upward turn at high luminosities is interpreted by Bernardi *et al.* as a signal of major mergers in the history of bright ellipticals. Our data does not confirm or falsify this conclusion. The shape of the CMR at the bright end appears to be independent of environment (De Propris, Phillip & Bremer 2013), supporting our old age, pure metallicity interpretation as the internal process of chemical enrichment dominates. The downturn they find at low luminosities is at the same luminosity that we find in our dwarf sample (first seen by Janz & Lisker 2009), thus they agree with our general observations of the low mass end. Another example of a blueward trend in the CMR at low luminosities is found in Agulli *et al.* (2016), who detect a blueward downturn for red sequence cluster members of Hercules (A2151). While they can not separate out galaxies by morphological, there is a clear trend for the

red sequence members of their spectroscopic survey to display bluer colors at luminosities fainter than -18 with respect to the expectation from a linear fit to the bright end of the CMR (see their Figure 1).

In contrast is the work of Roediger *et al.* (2016) who studied the CMR in Virgo down to $M_g = -9$. They do not identify a downward trend for dE's, but instead find a surprising flattening of color for galaxies fainter than -14 , well below our sample limit. It is difficult to make a comparison with our sample for their sample numbers are very low for ellipticals brighter than -18 (i.e., the normal elliptical CMR is ill-defined for their sample), and we have no ellipticals fainter than -14 in our sample. Their conclusions, that very low mass galaxies quench in star formation at the same epoch to produce similar colors, does not seem to apply to our dwarf ellipticals. A similar problem is found for a test of the linearity of the CMR in Virgo by Smith Castelli *et al.* (2013). In that study the focus was on the $g-z$ CMR of Virgo ellipticals between -16 and -20 . Again, the CMR is ill-defined with few bright ellipticals to stabilize the fitting of the high luminosity end. However, there was no evidence of a blueward trend between ellipticals brighter than -18 and those fainter than this demarcation.

Regardless of the filter combination, we confirm the main conclusion first expressed by Janz & Lisker (2009) that normal and dwarf ellipticals do not follow one, linear CMR. With the assumption that the deviation from normal elliptical CMR for dwarfs is real, and is systematic across the colors from *GALEX* to *WISE*, we present an interpretation based on a younger age for low mass ellipticals. We base this conclusion on the fact that the dE's deviate from the metallicity-color relations, defined by normal ellipticals, in a coherent fashion for each color combination. A trend that is predicted by SSP models, calibrated to globular cluster ages and metallicities, and indicates that the mean age of the stellar population in dwarf ellipticals is younger than normal ellipticals by between 2 to 8 Gyrs (younger with decreasing luminosity). With these younger ages, deduced metallicities range from -0.5 on the high mass side to -1.5 for the lower mass dwarfs, in agreement with the metallicities deduced from dwarf elliptical RGB CMD's (Caldwell 2006).

A younger mean age for dwarf ellipticals comes as no surprise given the detailed SFH results for M32, our nearest dE (Monachesi *et al.* 2011). To summarize the CMD results for M32, they find a mean metallicity of the RGB of -0.2 , but with a wide spread ranging from -1.0 to solar. Analysis of the red clump gives a mean age of 8 to 10 Gyrs (i.e., 2 Gyrs younger than normal ellipticals), but the detection of AGB stars above the RGB indicates some component of a 5 Gyr intermediate age population. Using a mass-weighted analysis, Monachesi *et al.* (2012) find 40% of the stellar population in M32 has an age between 2 and 5 Gyrs, with the remaining stars being older than 5 Gyrs for a average age of 7 Gyrs for all the stars. For the mean metallicity, this age agrees well with the color trend in Figure 8 where the dE's with $[\text{Fe}/\text{H}]$ values between -0.5 and solar have only slightly younger ages than normal ellipticals (in the 8 Gyrs range).

In a similar analysis, Mentz *et al.* (2016) find the age and metallicity of NGC1396 (a well-studied Fornax dE) to be -0.4 and 6 Gyrs. Geha *et al.* (2015) find values of

-1.0 and 10 Gyrs for NGC185 and -0.5 and 6 Gyrs for NGC147, the other two dE companions to M31. These values, and M32, are shown in Figure 8 and are consistent with the trend of luminosity and age for the entire dE sample. In addition, Rakos & Schombert (2004) found dE's are 3-4 Gyrs younger than bright ellipticals in Coma using narrow band continuum colors between 3500\AA and 5500\AA . Thus, a different age for stellar populations in dwarf ellipticals, compared to bright ellipticals, is well established.

Lastly, Sybilska *et al.* (2017) find, using SAURON results for 12 Virgo dE's, that their sample galaxies contain two stellar populations; an old (12 Gyrs) population and a younger (age < 5 Gyrs) population with varying degrees of dominance. They conclude they two populations are due to either extended SF (longer duration) or a second burst, leaning toward an extended SF interpretation. Range of ages presented by Sybilska *et al.* agrees well with our colors, although the $[\text{Fe}/\text{H}]$ values are much lower than we deduce from our multi-metallicity models.

It is important to note that assigning a mean age by color to dwarf ellipticals does not distinguish between a scenario where the initial epoch of star formation is at lower redshifts than normal ellipticals, or if that initial epoch was extending in duration such that the distribution of stellar ages peaks at the mean age value. In fact, the proposal by Thomas *et al.* (2005) based on spectral indices (particularly the α/Fe ratio), is that lower mass normal ellipticals have increasing SF duration times. Here the scenario is that all ellipticals have a common (and early) initial stage of SF, but lower mass normal ellipticals peak in star formation at later epochs (typically 2 to 3 Gyrs later than the most massive ellipticals). Given the information gleaned from a handful of nearby dwarf ellipticals that have high resolution CMD imaging, it appears that later scenario is more probable as a majority of these nearby dwarfs have a significant fraction of their stars in resolved old populations with ages greater than 10 Gyrs. Duration versus a later epoch of SF can be tested by color models; however, the α/Fe index is a more sensitive indicator of duration, at least for the first few Gyrs before Type I SN begin to enrich a galaxy with Fe.

In addition, there is no strong motivation to presume the SFH of dwarf ellipticals resembles normal ellipticals. Aside from their lack of visible structure (i.e., spiral arms) and no SF features (i.e., HII regions), the family of dE's has little else in common with normal ellipticals as they are structurally and kinematically distinct from the normal elliptical sequence (Schombert 2017). It also seems difficult to understand how normal ellipticals can be built from small objects like dE's or dIrr's given the differences in their stellar populations, unless this construction occurs at redshifts before the initial SF epoch. The fact that the mean age of dwarf ellipticals appears to approach the mean age of normal ellipticals at higher luminosities, in a smooth and uniform fashion (see Figure 8) suggests an independent process guides the SFH of dwarf ellipticals separate from the SFH process of ellipticals, but ends with similar patterns of SF at the highest dwarf masses.

The most commonly accepted evolutionary scenario for all types of galaxies since $z = 1$ is the so-called downsiz-

ing scenario (Gavazzi *et al.* 1996; Cowie *et al.* 1996), with massive galaxies forming the bulk of their stars in short, high star formation rates (SFR) periods at earlier epochs, whereas less-massive galaxies have delayed star formation histories which are extended over a longer time period (Gavazzi *et al.* 1996; Thomas *et al.* 2005; Nelan *et al.* 2005; Jimenez *et al.* 2007; Fontanot *et al.* 2009). In that limited context, the colors of dwarf ellipticals presented herein agree with that scenario. However, there is no evidence that normal ellipticals display any variation in age (although it is nearly impossible to distinguish an age change of less than 2 to 3 Gyrs from an old 12 Gyrs population). Recchi, Calura & Kroupa (2012) find the α/Fe index varies uniformly with stellar mass and also interpret this relationship as smaller galaxies forming over longer timescales (downsizing), allowing a larger amount of Fe (mostly produced by SN Ia) to be released and incorporated into newly forming stars. In addition, Fontana *et al.* (2004) find the typical M/L ratio of massive ellipticals is larger than that of less massive ones, suggesting that their stellar population formed at higher redshifts than dwarf ellipticals (see also Cappellari *et al.* 2013).

The mechanisms for halting star formation typical falls into two categories; quenching (Bundy *et al.* 2006) and exhaustion (Sánchez-Janssen *et al.* 2013). For normal ellipticals, who appear to have a majority of their stars in the form of an old, metal-rich population, their α/Fe ratios argues that an exhaustion process dominates. Presumably where the gas exhaustion is triggered by removal of large quantities by galactic winds (Matteucci 2004). For dwarf ellipticals, since their existence is strongly tied to a cluster environment (there are very few dE's in the field, Sandage, Binggeli & Tammann 1985), a quenching mechanism due to ram pressure stripping is implied. If the trend from Figure 8 is generic, then lower mass dwarf ellipticals have longer durations of initial SF and, therefore, younger mean ages than higher mass dwarf ellipticals, whose age and $[\text{Fe}/\text{H}]$ values continue the pure metallicity sequence of normal ellipticals. The age difference detected in dE colors is similar to the trend of age/metallicity seen in Peng, Maiolino & Cochrane (2015) study of SDSS galaxies.

The dilemma for a longer duration of SF for lower mass dE's is that longer timescales should produce higher metallicities, where the opposite is seen, the lowest mass dwarf ellipticals have the lowest metallicities. This presumes a SFR that is similar by mass. We can use the stellar mass-SFR correlation for LSB dwarfs from the SPARC dataset (Lelli, McGaugh & Schombert 2016) as a crude indicator of initial SFR. The so-called main sequence for LSB galaxies has a slope of unity with a typical SFR of $0.0003 M_{\odot}$ per yr^{-1} for stellar masses of $10^7 M_{\odot}$ rising to 0.04 at a stellar mass of $10^9 M_{\odot}$ (McGaugh, Schombert & Lelli 2017). Over durations of 8 to 2 Gyrs with increasing dE mass, this corresponds to between 10 and 25% the needed mass to make a present-day dwarf elliptical. Thus, the initial star formation rates would need to be only increased by a factor of 5 at early epochs to produce the objects we see today as quiescent dwarfs ellipticals. These low rates of star formation would inhibit chemical enrichment, and the deduced $[\text{Fe}/\text{H}]$ values for the dE's in this sample are only slightly metal richer than present-day LSB dwarfs of similar stel-

lar mass (Schombert & McGaugh 2015).

The last remaining question is what kind of galaxy, in terms of structure, would be produced from a history of early, but low level SF, which is halted suddenly by infall into the cluster environment? The presumption here is that LSB dwarfs and young dE's follow the same style of star formation at similar rates during the era of galaxy formation. The gas is converted into stars until the gas supply is exhausted (which has yet to happen for LSB dwarfs) or the gas supply is removed by tidal stripping (the probably event for cluster dE's to halt star formation). In this scenario, the stellar densities between LSB dwarfs and dE's should be similar with expected slightly higher central densities for dwarf ellipticals owing to a expected slightly higher SFR. Figure 9 displays this comparison using the central surface brightness of dwarf galaxies based on exponential fits. The LSB galaxies are taken from the SPARC sample (where $3.6\mu\text{m}$ mags are converted to W1 mags) and follow the same trend as dE's for absolute luminosity versus central surface brightness. The dwarf ellipticals are about 0.5 mags higher in central surface brightness compared to SPARC LSB's, but have similar central densities compared to the higher SFR sample from 11HUGS (Lee *et al.* 2007) and James *et al.* (2004). A KS test rejects the hypothesis that the dE and LSB samples are similar (the p-value was below 1%). Thus, the scenario proposed herein is that cluster dwarf ellipticals are cousins to field LSB dwarfs rather than high SFR BCD's or dIrr's. Their evolution was slightly faster in the past than current values for LSB galaxies, an evolution that was presumably cut short by entrance into a disruptive cluster environment where the gas supply was stripped and SF was halted. This scenario makes it difficult to assemble normal ellipticals from dwarf ellipticals, as their stellar populations have very different components, and will be a challenge for galaxy formation scenarios that depend on dry mergers.

Acknowledgements:

The author gratefully acknowledges numerous conversations with my SPARC colleagues, Stacy McGaugh and Federico Lelli. This project was motivated by discussions with Nelson Caldwell in the early 1980's. The software and funding for this project was supported by NASA's Applied Information Systems Research (AISR) and Astrophysics Data Analysis Program (ADAP) programs. Data used for this study was based on observations made with (1) the NASA Galaxy Evolution Explorer, GALEX is operated for NASA by the California Institute of Technology under NASA contract NAS5-98034, (2) SDSS where funding has been provided by the Alfred P. Sloan Foundation, the Participating Institutions, the National Science Foundation, the U.S. Department of Energy, the National Aeronautics and Space Administration, the Japanese Monbukagakusho, the Max Planck Society, and the Higher Education Funding Council for England, (3) the Wide-field Infrared Survey Explorer (WISE), which is a joint project of the University of California, Los Angeles, and the Jet Propulsion Laboratory/California Institute of Technology, funded by the National Aeronautics and Space Administration and (4) archival data obtained with the Spitzer Space Telescope, which is operated by the Jet Propulsion Laboratory, Cal-

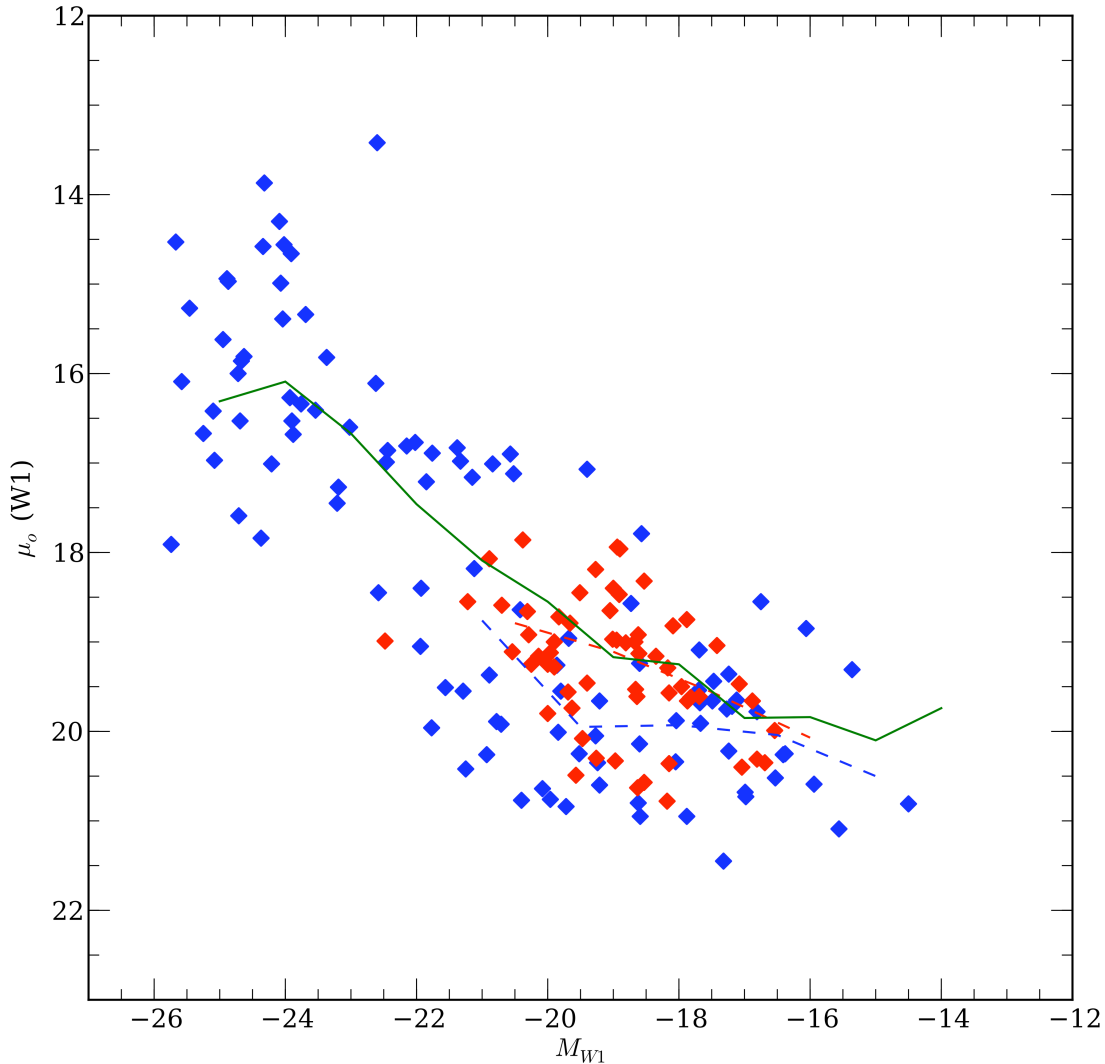


FIG. 9.— The relationship between total luminosity (i.e., total stellar mass at W1) and central surface brightness (μ_o) based on exponential fits to the W1 surface brightness profiles. The blue symbols are gas-rich LSB dwarfs from the SPARC database. Red symbols are the dwarf ellipticals from this study. The green line is a moving average of the 11HUGS and James *et al.* dataset for 462 late-type galaxies. The dashed lines are the moving average for the SPARC and dE samples. The dE's overlap the high SFR Irr sample of 11HUGS, and lie slightly higher in density than present-day LSB galaxies. The interpretation is that dE's had slightly higher SFR than present-day LSB's, resulting in slightly higher central stellar densities. However, the SF history of dE's would have been remarkably similar to present-day LSB's, i.e. slow, inhibited SF, until the cluster environment quenched the SF and removed the remaining gas. The low stellar densities and similar [Fe/H] values to present-day LSB's suggests a common star formation history.

ifornia Institute of Technology under a contract with NASA. In addition, this research has made use of the NASA/IPAC Extragalactic Database (NED) which is op-

erated by the Jet Propulsion Laboratory, California Institute of Technology, under contract with the National Aeronautics and Space Administration.

REFERENCES

- Agulli, I., Aguerri, J. A. L., Dominguez Palmero, L., & Diaferio, A. 2016, *MNRAS*, 461, L6
- Bernardi, M., Sheth, R. K., Annis, J., et al. 2003, *AJ*, 125, 1882
- Bernardi, M., Sheth, R. K., Nichol, R. C., Schneider, D. P., & Brinkmann, J. 2005, *AJ*, 129, 61
- Bernardi, M., Roche, N., Shankar, F., & Sheth, R. K. 2011, *MNRAS*, 412, 684
- Bouquin, A. Y. K., Gil de Paz, A., Boissier, S., et al. 2015, *ApJ*, 800, L19
- Bundy, K., Ellis, R. S., Conselice, C. J., et al. 2006, *ApJ*, 651, 120
- Caldwell, N. 1983, *AJ*, 88, 804
- Caldwell, N. 2006, *ApJ*, 651, 822
- Cappellari, M., McDermid, R. M., Alatalo, K., et al. 2013, *MNRAS*, 432, 1862
- Cardelli, J. A., Clayton, G. C., & Mathis, J. S. 1989, *ApJ*, 345, 245
- Cawson, M. G. M., Kibblewhite, E. J., Disney, M. J., & Phillipps, S. 1987, *MNRAS*, 224, 557
- Chang, R., Gallazzi, A., Kauffmann, G., et al. 2006, *MNRAS*, 366, 717
- Conroy, C., Graves, G. J., & van Dokkum, P. G. 2014, *ApJ*, 780, 33
- Cowie, L. L., Songaila, A., Hu, E. M., & Cohen, J. G. 1996, *AJ*, 112, 839
- Dabringhausen, J., & Fellhauer, M. 2016, *MNRAS*, 460, 4492

- De Propris, R., Phillipps, S., & Bremer, M. N. 2013, *MNRAS*, 434, 3469
- Driver, S. P. 2010, American Institute of Physics Conference Series, 1240, 17
- Egenthaler, P., & Zeilinger, W. W. 2013, *A&A*, 553, A99
- Faber, S. M., Trager, S. C., Gonzalez, J. J., & Worthey, G. 1995, *Stellar Populations*, 164, 249
- Fontana, A., Pozzetti, L., Donnarumma, I., et al. 2004, *A&A*, 424, 23
- Fontanot, F., De Lucia, G., Monaco, P., Somerville, R. S., & Santini, P. 2009, *MNRAS*, 397, 1776
- Gallazzi, A., Charlot, S., Brinchmann, J., White, S. D. M., & Tremonti, C. A. 2005, *MNRAS*, 362, 41
- Galleti, S., Bellazzini, M., Buzzoni, A., Federici, L., & Fusi Pecci, F. 2009, *A&A*, 508, 1285
- Gavazzi, G., & Boselli, A. 1996, New York: Gordon and Breach Science Publishers, —c1996, edited by Gavazzi, G.; Boselli, A., Graves, G. J., & Schiavon, R. P. 2008, *ApJS*, 177, 446-464
- Graves, G. J., Faber, S. M., & Schiavon, R. P. 2009, *ApJ*, 693, 486
- Graves, G. J., Faber, S. M., & Schiavon, R. P. 2010, *ApJ*, 721, 278
- Geha, M., Weisz, D., Grocholski, A., et al. 2015, *ApJ*, 811, 114
- Head, J. T. C. G., Lucey, J. R., Hudson, M. J., & Smith, R. J. 2014, *MNRAS*, 440, 1690
- James, P. A., Shane, N. S., Beckman, J. E., et al. 2004, *A&A*, 414, 23
- Janz, J., & Lisker, T. 2009, *ApJ*, 696, L102
- Jedrzejewski, R. I. 1987, *MNRAS*, 226, 747
- Jimenez, R., Bernardi, M., Haiman, Z., Panter, B., & Heavens, A. F. 2007, *ApJ*, 669, 947
- Johansson, J., Thomas, D., & Maraston, C. 2012, *MNRAS*, 421, 1908
- Kormendy, J., & Bender, R. 1996, *ApJ*, 464, L119
- Lee, J. C., Kennicutt, R. C., Funes, S. J., José G., Sakai, S., & Akiyama, S. 2007, *ApJ*, 671, L113
- Lelli, F., McGaugh, S. S., & Schombert, J. M. 2016, *AJ*, 152, 157
- Lisker, T., Grebel, E. K., & Binggeli, B. 2008, *AJ*, 135, 380
- Martin, C., & GALEX Team 2005, *Maps of the Cosmos*, 216, 221
- Matteucci, F. 2004, *Baryons in Dark Matter Halos*, 72.1
- Matteucci, F. 2007, *From Stars to Galaxies: Building the Pieces to Build Up the Universe*, 374, 89
- Mentz, J. J., La Barbera, F., Peletier, R. F., et al. 2016, *MNRAS*, 463, 2819
- Monachesi, A., Trager, S. C., Lauer, T. R., et al. 2011, *ApJ*, 727, 55
- Monachesi, A., Trager, S. C., Lauer, T. R., et al. 2012, *ApJ*, 745, 97
- Naab, T., Johansson, P. H., Ostriker, J. P., & Efstathiou, G. 2007, *ApJ*, 658, 710
- Nelan, J. E., Smith, R. J., Hudson, M. J., et al. 2005, *ApJ*, 632, 137
- Peacock, M. B., Maccarone, T. J., Knigge, C., et al. 2010, *MNRAS*, 402, 803
- Peng, Y., Maiolino, R., & Cochrane, R. 2015, *Nature*, 521, 192
- Powalka, M., Lançon, A., Puzia, T. H., et al. 2016, *ApJS*, 227, 12
- Rakos, K. D., & Schombert, J. M. 1995, *ApJ*, 439, 47
- Rakos, K., & Schombert, J. 2004, *AJ*, 127, 1502
- Rakos, K., Schombert, J., & Odell, A. 2008, *ApJ*, 677, 1019-1032
- Recchi, S., Calura, F., & Kroupa, P. 2012, *Astrophysics and Space Science Proceedings*, 28, 151
- Roediger, J. C., Ferrarese, L., Côté, P., et al. 2017, *ApJ*, 836, 120
- Sánchez-Janssen, R., Amorín, R., García-Vargas, M., et al. 2013, *A&A*, 554, A20
- Sandage, A., & Visvanathan, N. 1978, *ApJ*, 225, 742
- Sandage, A., Binggeli, B., & Tammann, G. A. 1985, *AJ*, 90, 1759
- Schawinski, K., Kaviraj, S., Khochfar, S., et al. 2007, *ApJS*, 173, 512
- Schombert, J., & McGaugh, S. 2014, *PASA*, 31, e036
- Schombert, J., & McGaugh, S. 2015, *AJ*, 150, 72
- Schombert, J., & Rakos, K. 2009, *ApJ*, 699, 1530
- Schombert, J., & Smith, A. K. 2012, *PASA*, 29, 174
- Schombert, J. 2007, *arXiv:astro-ph/0703646*
- Schombert, J., Maciel, T., & McGaugh, S. 2011, *Advances in Astronomy*, 2011, 143698
- Schombert, J. M. 2013, *PASA*, 30, e034
- Schombert, J. M. 2015, *AJ*, 150, 162
- Schombert, J. M. 2016, *AJ*, 152, 214
- Schombert, J. M. 2017, *PASA*, 34, e016
- Smith Castelli, A. V., González, N. M., Faifer, F. R., & Forte, J. C. 2013, *ApJ*, 772, 68
- Sybilaska, A., Lisker, T., Kuntschner, H., et al. 2017, *MNRAS*, 470, 815
- Thomas, D., Maraston, C., Bender, R., & Mendes de Oliveira, C. 2005, *ApJ*, 621, 673
- Tinsley, B. M. 1978, *Structure and Properties of Nearby Galaxies*, 77, 15
- Tojeiro, R., Masters, K. L., Richards, J., et al. 2013, *MNRAS*, 432, 359
- Trager, S. C., Faber, S. M., Worthey, G., & González, J. J. 2000, *AJ*, 120, 165
- Worthey, G. 1994, *ApJS*, 95, 107
- Worthey, G., Faber, S. M., Gonzalez, J. J., & Burstein, D. 1994, *ApJS*, 94, 687
- Worthey, G., Tang, B., & Serven, J. 2014, *ApJ*, 783, 20
- Wright, E. L., Eisenhardt, P. R. M., Mainzer, A. K., et al. 2010, *AJ*, 140, 1868-1881
- Yi, S., Demarque, P., & Oemler, A., Jr. 1998, *ApJ*, 492, 480
- de Vaucouleurs, G., de Vaucouleurs, A., Corwin, H. G., Jr., et al. 1991, *Third Reference Catalogue of Bright Galaxies*, by de Vaucouleurs, G.; de Vaucouleurs, A.; Corwin, H. G., Jr.; Buta, R. J.; Paturel, G.; Fouqué, P. Springer, New York, NY (USA), 1991, 2091